Observation-Based Estimates of Eulerian-Mean Boundary Downwelling in the Western Subpolar North Atlantic

Yingjie Liu, Damien Desbruyères, Herlé Mercier, Michael Spall

Observation-based estimates of Eulerian-mean boundary downwelling in the western subpolar North Atlantic

Y. J. Liu[1*], D. G. Desbruyères[1], H. Mercier[1] and M. A. Spall[2]

[1] University of Brest, CNRS, Ifremer, IRD, Laboratoire d'Océanographie Physique et Spatiale, UMR6523, IUEM, Ifremer centre de Brest, 29280 PLOUZANE, France

[2] Woods Hole Oceanographic Institution, Woods Hole, MA, USA

Corresponding author: Yingjie Liu (yingjie.liu@ifremer.fr)

Key Points:

- The long-term mean full-depth density field of the subpolar North Atlantic's boundary is reconstructed from hydrography data

- The along-boundary densification results in a 2.12 ± 0.43 Sv Eulerian-mean downwelling between Denmark Strait and Flemish Cap

- A first observation-based regional and seasonal distribution of near-boundary Eulerian-mean downwelling is provided

17 **Abstract**

18 A significant fraction of the Eulerian-mean downwelling feeding the lower limb of the Atlantic
19 Meridional Overturning Circulation (AMOC) occurs along the subpolar North Atlantic
20 continental slopes and is maintained by along-boundary densification and large-scale geostrophic
21 balance. We here use Argo and shipboard hydrography data to map the 2002-2015 long-term
22 mean density field along the boundary via a dedicated optimal interpolation tool. The overall
23 downstream densification implies an Eulerian-mean downwelling of 2.12 ± 0.43 Sv at 1100 m
24 depth between Denmark Strait and Flemish Cap. A clear regional pattern emerges with
25 downwelling in the Irminger Sea and western Labrador Sea and upwelling along Greenland
26 western continental slope. Comparisons with independent cross-basin estimates confirm that
27 vertical overturning transport across the marginal seas of the subpolar North Atlantic mainly
28 occurs along the continental slopes, and suggest the usefulness of hydrographic data in providing
29 quantitative information about the sinking branch of the AMOC.

30 **Plain Language Summary**

31 The Atlantic Meridional Overturning Circulation (AMOC), a critical component of the Earth's
32 climate system due to its role in redistributing heat and freshwater between low and high
33 latitudes, is anticipated to decline over the next century. The downwelling of surface waters in
34 the subpolar North Atlantic that feeds the lower limb of AMOC is a vital yet vulnerable process.
35 As revealed by previous theoretical and modelling work, the overall downstream densification
36 along the boundary results in a significant boundary downwelling. Here, the density along the
37 western boundary between Denmark Strait and Flemish Cap is reconstructed to provide a first
38 observation-based description of the regional and seasonal distribution of this boundary-focused
39 downwelling in the subpolar North Atlantic. This study not only provides valuable insights into
40 how to improve existing ocean circulation theories of overturning but also contributes to a solid
41 benchmark for evaluating how climate models simulate the sinking branch of the AMOC.
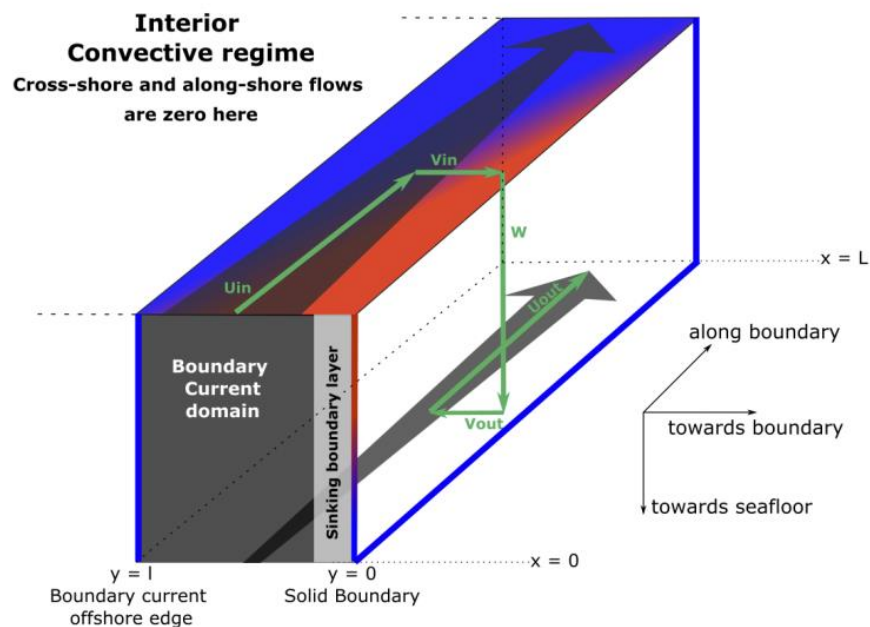
42 **1 Introduction**

43 Through its role in redistributing heat, freshwater, and chemical properties between low and high
44 latitudes, the Atlantic Meridional Overturning Circulation (AMOC) is a critical component of
45 Earth's climate system. Warm and saline waters flow from low latitudes towards the poles within
46 the AMOC upper limb. Following significant mixing-driven and surface-forced water mass
47 transformation, colder and fresher waters are returned southward as intermediate and deep-water
48 masses within the AMOC lower limb. Climate model studies indicate that the AMOC could
49 weaken significantly over the next century (IPCC, 2021), and significant efforts have been
50 consequently made over the last decades to understand the processes maintaining the AMOC and
51 the drivers of its variability (e.g., Lozier et al., 2012; Buckley and Marshall, 2016; Johnson et al.,
52 2019).

53 The vertical connection between the upper and lower limb of the AMOC, as well as the
54 underlying mechanism, are still under investigation (e.g., Spall & Pickart, 2001; Pedlosky, 2003;
55 Straneo, 2006; Spall, 2010; Brüggemann & Katsman, 2019). The location of this downwelling
56 has long been associated with regions of intense open-ocean convection, such as the Labrador
57 and Irminger seas, where dense and deep waters form because of convective mixing. However,
58 deep convection regions have large vertical heat and salt transports (in density space) but a
59 negligible vertical mass transport (in depth space) (Marshall and Schott 1999; Send and Marshall

60   1995; Spall 2003, 2004). Instead, the Eulerian−mean downwelling connecting the AMOC upper
61   and lower limbs should occur near continental boundaries, where geostrophy breaks down and a
62   new balance between vertical stretching of planetary vorticity and dissipation of relative vorticity
63   in a thin boundary layer emerges (Spall, 2010). Previous research has established that such
64   downwelling through modification of the boundary current properties in a region is undergoing
65   buoyancy loss (e.g., Spall & Pickart, 2001; Straneo, 2006; Spall, 2010; Cenedese, 2012; Katsman
66   et al., 2018). Notably, the dynamics of Eulerian-mean downwelling are primarily governed by
67   the large-scale geostrophic flow, so that the details of the thin boundary layer where vorticity is
68   ultimately dissipated do not need to be resolved for capturing the overall impact of downwelling
69   (Spall, 2008).

70   Several studies have focused on the location and underlying mechanism of boundary
71   downwelling. Spall and Pickart (2001) investigated the boundary sinking using a thermodynamic
72   balance. During winter, the boundary current loses heat and buoyancy. As shown schematically
73   in Figure 1, the resulting along-boundary density increase requires a vertically sheared cross-
74   shore baroclinic flow in thermal wind balance (V_{in}) fed by the boundary current itself (U_{in}; there
75   is no exchange with the basin interior). Therefore, the flow rotates counterclockwise with depth
76   along the boundary within a so-called "cooling spiral". To maintain local mass conservation, a
77   net downwelling (W) is required to balance the mass flux towards the boundary. This causes a
78   barotropization of the boundary current, with the upper part decelerating and the lower part
79   accelerating (Spall 2004, 2008; Straneo 2006). Without any mean mass flux between the
80   boundary region and the basin interior, the sinking water joins the lower part of the boundary
81   current (V_{out}) and is rapidly exported within the lower limb of AMOC (U_{out}). Thus, the along-
82   boundary pressure (or density) gradient and associated cross-shore geostrophic flow are vital for
83   sinking to occur.

84

85

Figure 1. The cooling spiral and associated boundary downwelling. Gray arrows represent the background boundary current. The blue-red shading depicts the horizontal density fields, with the distribution of light waters in red and dense waters in blue giving rise to a cross-shore baroclinic flow in thermal wind balance (V_{in}) fed by the boundary current (U_{in}). Local mass conservation lead to a downward flow at the wall (W), a deep entrainment in the boundary current (V_{out}), and a rapid along-boundary export (U_{out}). The overall effect in a net downwelling within and a barotropization of the boundary current.

Several processes, including surface buoyancy flux or mean and eddy-driven heat advection, likely contribute to maintaining an along-boundary density gradient. While the respective contribution of these processes is regionally unknown, lateral eddy-driven heat exchanges – generated by the lateral density gradients and baroclinic instability – are widely acknowledged as important in densifying the boundary region, as seen for instance in the Labrador Sea (Lilly et al., 2003; Katsman et al., 2004). Lateral eddy-induced heat fluxes are required to balance the heat loss to the atmosphere and restratify open-ocean water columns following deep convection events (Katsman et al., 2004; Hátún et al., 2007; Chanut et al., 2008; Kawasaki and Hasumi, 2014; Tagklis et al., 2020). Additionally, eddies contribute to interior downwelling and boundary current barotropization through along-isopycnal water masses stirring and exchange between the boundary current and the interior (Khatiwala and Visbeck, 2000; Brüggemann and Katsman, 2019).

Recent studies have used realistic and high-resolution model simulations to investigate the net downwelling in the entire Subpolar Gyre (SPG) (Katsman et al. 2018, Sayol et al. 2019) or in marginal seas characterized by high convective activity, such as the Labrador Sea (Brüggemann and Katsman 2019; Georgiou et al., 2019). Katsman et al. (2018) and Sayol et al. (2019) confirmed that the bulk of the vertical volume flux occurs along the boundary and that its spatial integral in the SPG is close to the magnitude of the AMOC – the zonally-integrated meridional flow – at the southern exit of the SPG (i.e., near 45°N). Katsman et al. (2018) further demonstrated that the amount of boundary sinking is largely determined by density change, except the region where eddy-driven processes or hydraulic controls may become significant. The role of eddy-driven processes was particularly studied by Brüggemann and Katsman (2019) and Georgiou et al. (2019), who showed the importance of eddies in balancing heat loss over the Labrador Sea and in triggering boundary downwelling along steepened isopycnal surfaces.

Estimates of boundary-focused sinking and its associated mechanisms from *in situ* observations are still lacking. Here, we use hydrography data from global ocean monitoring programs (e.g., Argo, Go-Ship) to estimate for the first time the long-term Eulerian-mean along-boundary downwelling and its spatial and seasonal distribution within the western SPG, from Denmark Strait (DKS) to Flemish Cap (FC). While such observations cannot resolve the intricate and small-scale dynamics of downwelling within the thin boundary layer where it is most likely to occur, they can be used to infer the large-scale geostrophic balance governing it.

We begin by introducing a specific optimal interpolation method to map temperature and salinity along the boundary, and then describe the method used for calculating cross-shore velocities and resulting vertical transport (section 2). Section 3 describes the reconstruction of the along-boundary density field, as well as the subsequent calculation of geostrophic velocity and associated downwelling. A summary and a discussion conclude this study (section 4).

129 **2 Data and Methodology**

130 2.1 Data

131 We use three datasets of temperature and salinity profiles to map the long-term mean (2002–
132 2015) and seasonal cycle of hydrographic properties in the SPG (52–66°N; 30°W–66°W): the In
133 Situ Analysis System-ISAS15 (Kolodziejczyk et al., 2021; Gaillard et al., 2016), the Coriolis
134 data set for ReAnalysis-CORA (Szekely et al., 2019; Cabanes et al., 2013), and EN4.4.2.2 (Good
135 et al., 2013). Whereas ISAS15 only contains Argo profiles, EN4 and CORA include profiles
136 from fixed moorings and shipboard full-depth CTD profiles. These profiles have undergone
137 quality control checks in delayed mode, and we only use *good* profiles (i.e., fully acceptable).
138 Because most of Argo floats drift at 1000 m depth, ISAS15 exhibits an uneven distribution
139 across the domain with decreasing near the shelf (see Figure S1). The EN4 and CORA provide
140 adequate coverage of profiles near the shelf. The temperature and salinity fields are then used to
141 derive the in situ (ρ) and potential (σ_0) density fields. Bathymetry is derived from ETOPO2.

142 2.2 Optimal Interpolation

143 Optimal interpolation (OI) is a frequently used technique for generating gridded property fields
144 from sparse and irregular data (Bretherton et al., 1976, Kaplan et al., 1997). The conventional OI
145 algorithms for climatological mapping use circle-shaped Gaussian correlation functions (see
146 Gaillard et al., 2016 for additional details), but we herein employ an elliptic Gaussian correlation
147 function parallel to isobaths, with length scales of 67 km (cross-shore axis) and 145 km (along-
148 shore axis) to account for the larger (smaller) correlation length scales in the along-shore (cross-
149 shore) directions. In other words, this provides data along the boundary current's primary path
150 larger weights in the estimation. Based on convergence sensitivity tests, the horizontal resolution
151 is set as 4km, which enables us to refine the properties along boundaries and topographic
152 features (such as the sharpest portions of the continental slope). Interpolation is conducted at 152
153 levels independently between 0 and 2000 m; the vertical spacing is 5 m down to 100 m, 10 m
154 down to 800 m, and 20 m below. The configuration of the OI is explained in more detail in
155 Gaillard et al., (2016). The overall mapping methodology was eventually validated by good
156 performance in estimating properties along the OVIDE and AR7W hydrographic lines (see
157 Figure S2-S5). To estimate the vertical transport, the final multiproduct mappings of temperature
158 and salinity for the four seasons (Winter (Jan-Mar), Spring (Apr-Jun), Summer (Jul-Sep),
159 Autumn (Oct-Dec)) is the average of the fields derived independently from the three datasets.
160 The density below 2000 m is obtained by linear extrapolation from the above 2000 m. The three-
161 dimensional density field is eventually interpolated onto the locations of 100m-spaced isobaths
162 spanning 700 m to 3000m from DKS to FC.

163 2.3 Computing cross-shore geostrophic velocity and the vertical transport

164 To calculate the absolute geostrophic cross-shore velocity, a local mass balance assumes equal
165 inshore and offshore transport. Any horizontal recirculations between the boundary current and
166 the interior are assumed to be mostly barotropic, with no effect on the cross-shore baroclinic
167 density field. These assumptions are supported by laboratory experiments showing that water
168 downwelling along a vertical wall returns offshore in the opposite direction (Cenedese, 2012),
169 and by observations of the strong barotropic nature of inner gyres and lateral entrainments (Våge
170 et al., 2011). The baroclinic component of the cross-shore velocity relative to the sea surface

171 ($v_{baroclinic}$) is firstly derived from the along-boundary density gradient and the thermal wind
172 balance:

$$\frac{\partial v_{baroclinic}(x,y,z)}{\partial z} = -\frac{g}{\rho_0 f}\frac{\partial \rho(x,y,z)}{\partial x} \qquad (1)$$

174

175 where x, y, and z represent the along-shore, cross-shore, and vertical directions, respectively. ρ
176 is the *in-situ* density field derived from OI, ρ_0 is 1024 kg/m^3, and f is 1.26×10^{-4} s^{-1}.
177 The reference velocity $v_{reference}$ is then obtained by applying the local *zero-mass transport*
178 *constraint*:

$$v_{reference}(x,y) = \frac{-\int_{H(x,y)}^{0}\left(v_{baroclinic}(x,y,z)\right)dz}{\Delta z} \qquad (2)$$

179

180 where H (x,y) denotes the bottom depth and Δz the water depth.

181

182 We calculate vertical transport along the SPG at isobaths ranging from 700 to 3000 m with a
183 100-meter interval. The analysis focuses offshore of the 700 m isobath because of poorer
184 sampling inshore. This has little effect on the maximum transport estimate, however, which is
185 found across much deeper slope. For a given isobath (y_0), the vertical transport streamfunction
186 $\psi(z)$ is estimated as follows:

$$\psi(y_0, z) = \int_{x_u}^{x_d}\int_{z}^{0}\left(v_{baroclinic}(x,y_0,z') + v_{reference}(x,y_0)\right)dz'dx \qquad (3)$$
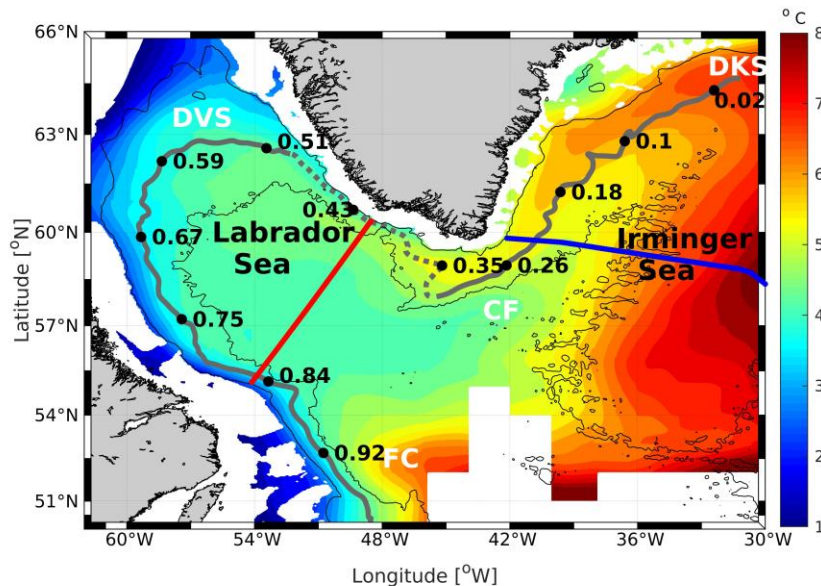
187

188

189 where x_u and x_d are the upstream and downstream locations along a given isobath y_0. The
190 maximum of $\psi(y_0, z)$ represents the net shoreward transport integrated along an isobath between
191 x_u and x_d. The maximum vertical transport is thus defined as the maximum of the net shoreward
192 transport ψ_{max} across the 100-m spaced isobaths between 700 m and 3000 m.

193

194 A Monte Carlo approach is used to add an uncertainty estimate to our mean vertical transport
195 calculation. We use the errors estimated from the OI calculation, which depend on the
196 distribution density and variability of adjacent profiles, to perturb the temperature and salinity
197 fields randomly and re-compute overturning streamfunctions. 12000 bootstrap estimates of the
198 streamfunctions in four seasons are calculated using 3000 iterations on the three datasets. The
199 errors of the transport are considered as two times the standard deviation of the 12000 estimates
200 (see Figure S6).

201 **3 Results**

202 Figure 2 shows the multiproduct long-term mean temperature field averaged over the upper 300
203 m depth. It depicts the cooling of the warm boundary current in the upper layer as it flows from
204 DKS to FC. The full-depth surface-referenced in situ (ρ) and potential (σ_0) fields are determined
205 along 100 m-spaced isobaths ranging from 700 to 3000m. The 2400m isobath is shown here (for
206 the reason that will become obvious later) and labeled using the distance relative to the isobath's
207 total length (4032 km), starting at s=0 near the DKS at -30°W and ending at s=1 near FC at -
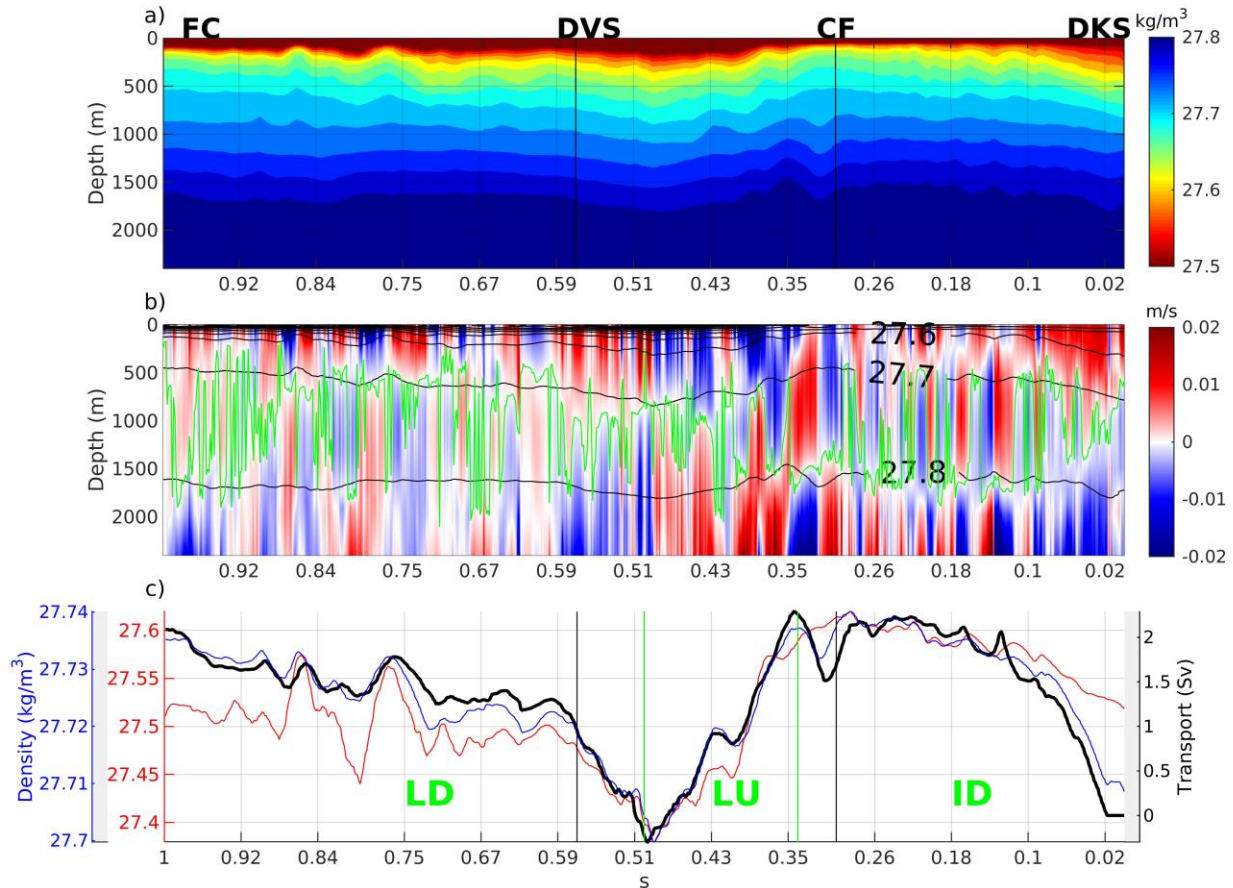208 48°W.

209
210

211

Figure 2. Observed multiproduct time-mean (2002-2015) temperature field averaged in upper 300 m as obtained from an OI tool specifically designed for the boundary region (see section 2.2). The isobaths 700 m and 3000 m are shown as thin black contours, and the isobath 2400 m (thick black line) used in Figure 3 to show along-boundary density and velocity fields, from s = 0 at Denmark Strait until s = 1 at Flemish Cap. Solid and dashed portions of this contour refer to (Eulerian) downwelling and upwelling regions. Key locations noted in the plot are Denmark Strait (DKS), Cape Farewell (CF), Davis Strait (DVS), and Flemish Cape (FC). Red line indicates the AR7W section, whereas the blue line indicates the OVIDE section.

Figure 3ab depicts the density and associated cross-shore geostrophic velocity sections following isobath 2400 m from DKS to FC (the along-isobath baroclinic and reference velocities in Equation 2 are shown in Figure S8). The density generally increases downstream (Figure 3a, c) and is primarily determined by the change in along-shore temperature (see Figure S7). The density of the upper (above 300m) and intermediate layer (300-1500 m) gradually increases from s=0 to s=0.3, while it decreases from s = 0.3 until the east of Davis Strait (DVS) (s=0.5) (Figure3c). Downstream of DVS, the density in the intermediate layer increases again but remains constant in the upper layer. Overall, even though the density in the upper layer remains constant, the increase in density in the intermediate layer along isobath 2400 m from 27.71 kg m^{-3} to 27.74 kg m^{-3} should expectedly drive an overall downwelling. The resulting cross-shore absolute geostrophic velocity (Figure 3b) shows the water flows inshore (offshore) and offshore (inshore) in the upper and lower layers, driving downwelling (upwelling). There are two levels of no motion at some boundary locations due to more complex changes of stratification (induced by the freshwater inflow near DVS, for instance). The level of no motion is deeper in the Irminger Sea than in the Labrador Sea and ranges from 500 to 1500m depth.
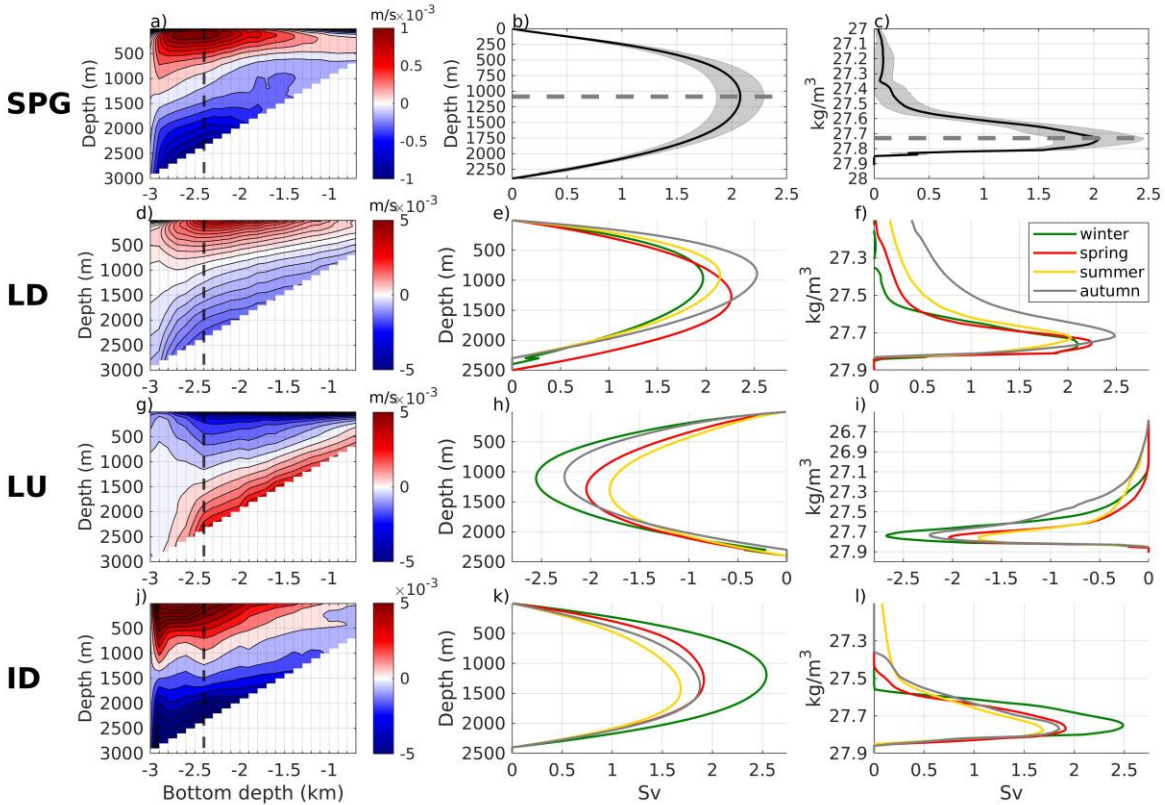
236

Figure 3. (a) OI-derived multiproduct density (σ_0) field along isobath 2400 m. (b) The cross-shore geostrophic velocity field along isobath 2400 m. The positive (negative) values indicate inshore (offshore) flows. The green line indicates the depth at which the maximum (accumulated) vertical transport is found (i.e., levels of no motion). The σ_o=27.6, 27.7, 27.8 kg m^{-3} isopycnals are contoured in black. (c) The density along the boundary from s = 0 to s = 1 averaged in the upper layer (1-300m, red curve) and the intermediate layer (301-1500m, blue curve). The maximum vertical transport (black curve) accumulated along the boundary from s = 0 to s = 1. The upward slopes indicate the downwelling (LD-Labrador Downwelling, s = 0.5~1, ID-Irminger Downwelling, s = 0~0.33), and the downward slope indicates upwelling (LU-Labrador Upwelling, s = 0.33~0.5).

A vertical section of the DKS-FC along-shore average of the cross-shore velocity crossing different isobaths is shown in Figure 4a. It reveals a cell-like structure in the upper and lower layers, with a cell center in the isobath 2400 m at 100 m depth. In line with theory and experimental works (Spall, 2008 and Cenedese, 2012), the cross-shore velocity increases from the coast offshore to a maximum near the 2400 m isobath and then decreases offshore until the along-shore density gradient becomes insignificant at circa the 3000 m isobath. The mean maximum vertical transport along the SPG boundary is 2.12 Sv at 1088 m, with an uncertainty of 0.43 Sv (2 times STD) estimated from 12000 bootstrap estimates. The transport in density space is 2.11 ± 0.28 Sv by crossing the nearly-horizontal 27.73 kg/m^3 isopycnal surface. Note that this

258   does not fully account for water mass formation near the boundary since the diapycnal flux is
259   also carried out by the along-stream densification in the upper layer and cross-stream eddy
260   circulation in the deeper layer (Brüggemann & Katsman, 2019).
261

262

Figure 4. (a) The along-shore average of the cross-shore velocity along the SPG averaged at the
100 m-spaced isobaths between 700 m and 3000 m. The x-axis represents distinct isobaths rather
than the cross-shore distance. The dashed line indicates the isobath (2400m) where the maximum
vertical transport is found. (b)(c) The corresponding geostrophic streamfunctions obtained by
accumulating the vertical transport from the surface in depth space and density space. The errors
in gray patch are one standard deviation derived from the bootstrap simulations. The dashed lines
indicate the depth (density) of maximum overturning. Panels (d)-(l) are the same as (a)-(c), but
for the three regions defined in Figure 1 and Figure 2c and for the four seasons: Winter (Jan-
Mar), Spring (Apr-Jun), Summer (Jul-Sep), Autumn (Oct-Dec). The uncertainty estimates and
maximum overturning depths for each region are represented in Table 1.

273

The cumulative transport (Figure 3c) along the 2400 m isobath reveals that the entire DKS-FC
boundary can be divided into three distinct areas: a downwelling region in the Irminger Sea (ID,
s=0 to s=0.33), an upwelling region in the eastern Labrador Sea (LU, s=0.33 to s=0.5), and a
downwelling region in the western Labrador Sea (LD, s=0.5 to s=1). These
downwelling/upwelling patterns result from the downstream density increase/decrease along the
boundary (Figure 3a). The cross-shore velocities averaged along the isobaths in these
three regions are shown in Figure 4dgj. They also capture cell-like structures within the
boundary current system, with waters flowing inshore (offshore) in the upper layer and offshore

282 (inshore) in the lower layer of the downwelling (upwelling) region. Maximum cross-
283 shore transports, which are consistently observed at the 2400-m isobath, are of comparable
284 magnitude in each of the three regions with upwelling (2.17 Sv) along the western slope of
285 Greenland balancing half of the total downwelling (4.28 Sv) (Figure 4ehk).

286

287 Water sinks (upwells) all year in the downwelling (upwelling) regions. The Eulerian-mean
288 transport in the LD region is 2.23±0.71 Sv (Figure 4e and Table 1) at a depth of 986 m. The
289 transport in the LU region (Figure 4h and Table 1) is 2.17±0.74 Sv at a depth of 1182 m. The ID
290 has similar downwelling of 2.05±0.79 Sv to the LD (Figure 4k and Table 1) at a depth of 1304
291 m. The regional density-space transport follows a very similar pattern to that in depth-space, and
292 the density level of maximum transport remains nearly constant at around 27.71 to 27.76 kg/m3.
293 The uncertainty estimates in Table 1 show the standard deviations calculated from 3000
294 iterations using the three datasets. Seasonal and regional errors are all between 0.3 and 0.8 Sv.
295 The seasonal variations are of the same magnitude as the uncertainties derived from the bootstrap
296 estimates based on the three datasets, and the present estimates of seasonal changes of the
297 Eulerian-mean downwelling are not statistically significant for the whole SPG or individual
298 basins. This is in line with Li et al., (2021) who did not detect a statistically significant signal
299 cycle when estimating the composite monthly mean MOC transport using the OSNAP program's
300 46-month records. Furthermore, Sayol et al. (2019) used a high-resolution model to find that
301 seasonal variability in boundary sinking is rather insignificant in comparison to interior sinking,
302 and that the variability is thought to be driven by ageostrophic dynamics that our large-scale
303 geostrophic balance cannot capture. Nevertheless, based on our observations, a potential upper
304 bound on the seasonal cycle amplitude has been established.

305
306

Season	LD	LU	ID	SPG
Winter	1.97±0.30 (970)	-2.56±0.44 (1108)	2.57±0.31 (1190)	**1.99±0.58** (975)
Spring	2.27±0.31 (1274)	-2.04±0.31 (1288)	1.92±0.61 (1278)	**2.14±0.81** (1253)
Summer	2.16±0.28 (923)	-1.81±0.34 (1301)	1.84±0.84 (1425)	**2.19±0.82** (903)
Autumn	2.54±0.51 (891)	-2.27±0.60 (1084)	1.88±0.45 (1372)	**2.14±0.47** (1044)
Annual	**2.23±0.71 (986)**	**-2.17±0.74** (1182)	**2.05±0.79** (1304)	**2.12±0.43** (1088)

307 Table 1. The maximum vertical transport (Sv) derived from the multiproduct mean in the LD,
308 LU and ID regions (defined in Figure 2) and whole SPG. The errors are two times of standard
309 deviation derived from the bootstrap simulations. The depths (m) of the maximum transport are
310 displayed in parentheses.

311

4 Discussion and Conclusion

313 We have provided here a first observation-based estimate of the Eulerian-mean downwelling
314 along the boundary of the SPG. Using *in situ* temperature and salinity profiles from sustained
315 global ocean observational networks, we mapped the long-term mean density along the
316 continental slope from the Denmark Strait to Flemish Cap. The cooling and resulting
317 densification along the boundary region result in a geostrophic cross-shore flow and a
318 downwelling above the continental slope, with a maximum value of 2.12 ± 0.43 Sv at 1100 m
319 depth. The transport in density space, which is here representative of the cross-shore diapycnal
320 flux, is very similar to the transport in depth space. Cross-shore velocity is found to increase

321 offshore and peak near the 2400 m isobath, before eventually disappearing near the 3000m
322 isobath, in good agreement with observation-based descriptions of the distinct circulation of the
323 interior and the boundary current (Pacini et al., 2020), and with theoretical or modelling works
324 suggesting limited mean advective exchanges between those two regimes (Cenedese, 2012;
325 Brüggemann and Katsman 2019). Our analysis further reveals no strong or statistically
326 significant seasonality in the magnitude of downwelling across the entire SPG.

327

328 Interestingly, the total Eulerian-mean downwelling from CF to FC is estimated as only 0.1±0.03
329 Sv due to compensation between upwelling along the western slope of Greenland and
330 downwelling in the remaining portion of the Labrador Sea. Downwelling was estimated to be 1.4
331 Sv in that region by Katsman et al. (2018) in high-resolution simulations. Western Greenland is
332 in fact generally described as a region with strong along-shore densification due notably to eddy-
333 driven heat flux, as described in several modelling works (Katsman et al., 2004; Georgiou et al.,
334 2019). This apparent discrepancy could arise for several reasons. Warming in the intermediate
335 layer might be overly represented due to an uneven distribution of profiles along western
336 Greenland's narrowing boundary, which may be insufficient to represent the boundary current's
337 features. It is also possible that the subsurface warming along western Greenland (also observed
338 in other estimates, see, e.g., Palter et al., 2008) indicates a signal of restratification following
339 baroclinic instability. The tilted isopycnals on the offshore side of an unstable current should
340 deepen downstream and drive a warming signal in this portion of the water column.
341 Additionally, the cross-shore transport along the narrowing boundary might represent the
342 deflection of upper layer water into the interior. An offshore mass flux, resulting from either a
343 flux of less dense water off the shelf or a broadening of the boundary current due to baroclinic
344 instability, would be diagnosed as upwelling because of the assumption of no net flow across the
345 isobaths. Future work may focus on describing the properties in shallower depths further inshore
346 when sampling is denser. Nevertheless, the net downwelling in SPG is not sensitivity to the
347 distribution of boundary downwelling or upwelling, as demonstrated by the fact that the strong
348 downstream warming and subsequent upwelling in the eastern Labrador Sea are compensated by
349 the significant downstream cooling and subsequent downwelling in the western Labrador Sea.
350 Indeed, the full-basin integrated downwelling only depends on the density variation between the
351 DKS and FC and thus remains a robust estimate.

352

353 Further comparison with independent overturning estimates from cross-basin arrays or realistic
354 modelling provides insights and confidence in the values reported herein. The Irminger Sea
355 downwelling is estimated to be 2.05±0.79 Sv at 1200 m depth, in line with the high-resolution
356 modelling estimates of 1.4 Sv from Katsman et al. (2018) and 1.13 Sv from Sayol et al. (2019).
357 Summer downwelling in the Labrador Sea is estimated to be 0.85±0.15 Sv at depth 685 m by
358 integrating the transport between the two ends of the AR7W line (Figure 2), which agrees
359 quantitatively with Pickart and Spall' s (2007) observation-based meridional transports of about 1
360 Sv at depth 800 m. The annual mean downwelling rate in the Labrador Sea is estimated here as
361 0.72±0.07 Sv, similar to Holte and Straneo's (2017) and Lozier et al. (2019) estimates, which
362 amount to 0.9 Sv and 0.8 Sv, respectively. This also confirms that the majority of sinking occurs
363 near the Labrador Sea's boundary, with little vertical mass transport occurring in the convective
364 interior.

365

Furthermore, we quantify here only the western boundary downwelling downstream of DKS, omitting potential upstream contributions around Reykjanes Ridge (RR) or the Rockall Plateau, for instance. The zero-mass constraint used herein to estimate cross-shore overturning is likely inadequate in such regions where the vertical integral of the cross-shore geostrophic flow is not zero (consider for instance the net westward flow above the crest of RR). Additionally, overflows across the DKS or the Iceland-Scotland Ridge contribute significantly to the overall net sinking in the SPG – about 7 Sv (Hansen & Østerhus, 2000) – via hydraulically-controlled dynamics not captured by our geostrophic estimate. A refinement of the boundary sinking calculation is being investigated for these specific areas.

Ekman transport was estimated from the long-term mean (2002-2015) along-shore wind stress averaged from the NCEP/NCAR Reanalysis 1 and ERA5 dataset. It carries 0.7 to 0.9 Sv of water inshore of the DKS-FC boundary. Two-dimensional models require that this onshore flow returns to the basin interior (e.g. Lentz and Chapman, 2004; Choboter et al., 2011), but three-dimensional models with spatially variable winds (or coastlines) demonstrate that some of this water flows along the shelf (e.g. Allen, 1976; Suginohara, 1982). It is difficult to determine a priori the partition of this downwelled water between along-shelf and interior pathways as it will depend on various factors such as stratification, topography, nonlinearity, wind pattern, etc. However, any of the Ekman transport that does flow back into the interior will remain relatively shallow and have a negligible effect on the deep overturning circulation, and so is not included in our estimate.

We finally emphasize that novel descriptions of the Eulerian-mean downwelling rooted in observations are critical for understanding AMOC variability in the current context of anthropogenic climate change (IPCC, 2021). Both upper-ocean warming and increased ice melting may significantly affect along-boundary density gradients and result in the reduced sinking and a consequent weakening of the AMOC. A better observation-based understanding of boundary-focused vertical transport may also help us to properly represent or parameterize the details of the underlying boundary dynamics in climate models. It can assist in not only describing the circulation and diagnosing its controls, but also in providing valuable insights into how to improve existing ocean circulation theories of overturning.

Data Availability Statement

The In Situ Analysis System-ISAS15 dataset (2002-2015) is available from the SEANOE repository (https://www.seanoe.org/data/00412/52367/, last access: July 2021) and described in Gaillard et al. (2016). The Coriolis data set for ReAnalysis-CORA V5.2 (1950-to present) is available from the SEANOE repository (https://www.seanoe.org/data/00351/46219/, last access: September 2019) and described in Szekely et al. (2016). The EN4.4.2.2 dataset for years 1990 to present is provided by Met Office Hadley Centre and available at https://www.metoffice.gov.uk/hadobs/en4/ (last access: November 2021) and described in Good et al. (2013). The A25-Ovide and AR7W hydrography sections are available via the CLIVAR and Carbon Hydrographic Data Office (CCHDO) platform (https://cchdo.ucsd.edu/). The NCEP/NCAR Reanalysis 1 (1948/01/01 to present) is provided in National Centers for Environmental Prediction (/data/gridded/data.ncep.reanalysis.html). The ERA5 dataset (1950-to present) is available in Copernicus Climate Change Service Climate Data Store (CDS),

https://cds.climate.copernicus.eu/cdsapp#!/home. The present analysis does not use new unpublished data.

References

Allen, J. S., 1976: Some aspects of the forced wave response of stratified coastal regions. *Journal of Physical Oceanography*, 6, 113-119

Bretherton, F. P., Davis, R. E., and Fandry, C. B. (1976). A technique for objective analysis and design of oceanographic experiments applied to MODE-73. *Deep Sea Res*. 23, 559–582. doi: 10.1016/0011-7471(76)90001-2

Brüggemann, N., & Katsman, C. A. (2019). Dynamics of downwelling in an eddying marginal sea: Contrasting the eulerian and the isopycnal perspective. *Journal of Physical Oceanography*, *49*(11), 3017–3035. https://doi.org/10.1175/JPO-D-19-0090.1

Buckley,M.W., and Marshall, J. (2016).Observations, inferences, and mechanisms of Atlantic meridional overturning circulation variability: a review. Rev. Geophys. 54, 5–63. doi: 10.1002/2015RG000493

Cabanes, C., Grouazel, A., Von Schuckmann, K., Hamon, M., Turpin, V., Coatanoan, C., et al. (2013). The CORA dataset: Validation and diagnostics of in-situ ocean temperature and salinity measurements. *Ocean Science*, 9(1), 1–18. https://doi.org/10.5194/os-9-1-2013

Cenedese, C. (2012). Downwelling in basins subject to buoyancy loss. *Journal of Physical Oceanography*, *42*(11), 1817–1833. https://doi.org/10.1175/JPO-D-11-0114.1

Cessi, P., Wolfe, C. L., & Ludka, B. C. (2010). Eastern-boundary contribution to the residual and meridional overturning circulations. Journal of Physical Oceanography, 40(9), 2075–2090. https://doi.org/10.1175/2010JPO4426.1

Chanut, J., Barńier, B., Large, W., Debreu, L., Penduff, T., Molines, J. M., & Mathiot, P. (2008). Mesoscale eddies in the Labrador Sea and their contribution to convection and restratification. Journal of Physical Oceanography, 38(8), 1617–1643. https://doi.org/10.1175/2008JPO3485.1

Choboter, P. F., Duke, D., Horton, J. P., & Sinz, P. (2011). Exact solutions of wind-driven coastal upwelling and downwelling over sloping topography. Journal of Physical Oceanography, 41(7), 1277–1296. https://doi.org/10.1175/2011JPO4527.1

Copernicus Climate Change Service (C3S) (2017): ERA5: Fifth generation of ECMWF atmospheric reanalyses of the global climate . Copernicus Climate Change Service Climate Data Store (CDS), date of access. https://cds.climate.copernicus.eu/cdsapp#!/home

EN.4.2.2 data were obtained from https://www.metoffice.gov.uk/hadobs/en4/ and are © British Crown Copyright, Met Office, [2021], provided under a Non-Commercial Government Licence http://www.nationalarchives.gov.uk/doc/non-commercial-government-licence/version/2/

Gaillard, F., Reynaud, T., Thierry, V., Kolodziejczyk, N., & Von Schuckmann, K. (2016). In situ-based reanalysis of the global ocean temperature and salinity with ISAS: Variability of the heat content and steric height. *Journal of Climate*, 29(4), 1305–1323. https://doi.org/10.1175/JCLI-D-15-0028.1

Georgiou, S., van der Boog, C. G., Brüggemann, N., Ypma, S. L., Pietrzak, J. D., & Katsman, C. A. (2019). On the interplay between downwelling, deep convection and mesoscale eddies in the Labrador Sea. *Ocean Modelling*, *135*, 56–70. https://doi.org/10.1016/j.ocemod.2019.02.004

Good, S. A., M. J. Martin and N. A. Rayner, 2013. EN4: quality controlled ocean temperature

and salinity profiles and monthly objective analyses with uncertainty estimates, *Journal of Geophysical Research: Oceans*, doi:10.1002/2013JC009067

Hansen, B., & Østerhus, S. (2000). North Atlantic-Nordic Seas exchanges. Progress in Oceanography, 45(2), 109–208. https://doi.org/10.1016/S0079-6611(99)00052-X

Hátún, H., Eriksen, C. C., & Rhines, P. B. (2007). Buoyant eddies entering the Labrador Sea observed with gliders and altimetry. *Journal of Physical Oceanography*, *37*(12), 2838–2854. https://doi.org/10.1175/2007JPO3567.1

Holte, J., & Straneo, F. (2017). Seasonal overturning of the Labrador sea as observed by Argo floats. *Journal of Physical Oceanography*, *47*(10), 2531–2543. https://doi.org/10.1175/JPO-D-17-0051.1

IPCC, 2021: Climate Change 2021: The Physical Science Basis. Contribution of Working Group I to the Sixth Assessment Report of the Intergovernmental Panel on Climate Change [Masson-Delmotte, V., P. Zhai, A. Pirani, S.L. Connors, C. Péan, S. Berger, N. Caud, Y. Chen, L. Goldfarb, M.I. Gomis, M. Huang, K. Leitzell, E. Lonnoy, J.B.R. Matthews, T.K. Maycock, T. Waterfield, O. Yelekçi, R. Yu, and B. Zhou (eds.)]. Cambridge University Press.

Johnson, H. L., Cessi, P., Marshall, D. P., Schloesser, F., & Spall, M. A. (2019). Recent Contributions of Theory to Our Understanding of the Atlantic Meridional Overturning Circulation. In *Journal of Geophysical Research: Oceans* (Vol. 124, Issue 8, pp. 5376–5399). Blackwell Publishing Ltd. https://doi.org/10.1029/2019JC015330

Kaplan, A., Kushnir, Y., Cane, M., and Blumenthal, B.: Reduced space optimal analysis for historical data sets: 136 years of Atlantic sea surface temperature, *Journal of Geophysical Research: Oceans*, 102, 27 853–27 860, 1997

Katsman, C. A., Drijfhout, S. S., Dijkstra, H. A., & Spall, M. A. (2018). Sinking of dense north atlantic waters in a global ocean model: Location and controls. *Journal of Geophysical Research: Oceans*, *123*(5), 3563–3576. https://doi.org/10.1029/2017JC013329

Katsman, Caroline A, Spall, M. A., & Pickart, R. S. (2004). Boundary Current Eddies and Their Role in the Restratification of the Labrador Sea. *Journal of Physical Oceanography*, *34*(9), 1967–1983. https://doi.org/10.1175/1520-0485(2004)034<1967:BCEATR>2.0.CO;2

Kawasaki, T., & Hasumi, H. (2014). Effect of freshwater from the West Greenland Current on the winter deep convection in the Labrador Sea. *Ocean Modelling*, *75*, 51–64. https://doi.org/10.1016/j.ocemod.2014.01.003

Khatiwala, S., & Visbeck, M. (2000). An estimate of the eddy-induced circulation in the Labrador Sea. *Geophysical Research Letters*, *27*(15), 2277–2280. https://doi.org/10.1029/1999GL011073

Kolodziejczyk N., Prigent-Mazella A., Gaillard F. (2021). ISAS temperature and salinity gridded fields. SEANOE. https://doi.org/10.17882/52367

Lentz, S. J., & Chapman, D. C. (2004). The importance of nonlinear cross-shelf momentum flux during wind-driven coastal upwelling. *Journal of Physical Oceanography*, 34(11), 2444–2457. https://doi.org/10.1175/JPO2644

Li, F., Lozier, M. S., Bacon, S., Bower, A. S., Cunningham, S. A., de Jong, M. F., deYoung, B., Fraser, N., Fried, N., Han, G., Holliday, N. P., Holte, J., Houpert, L., Inall, M. E., Johns, W. E., Jones, S., Johnson, C., Karstensen, J., Le Bras, I. A., … Zhou, C. (2021). Subpolar North Atlantic western boundary density anomalies and the Meridional Overturning Circulation. *Nature Communications*, *12*(1). https://doi.org/10.1038/s41467-021-23350-2

Lilly, J. M., Rhines, P. B., Schott, F., Lavender, K., Lazier, J., Send, U., & D'Asaro, E. (2003).

502   Observations of the Labrador Sea eddy field. In *Progress in Oceanography* (Vol. 59, Issue
503   1, pp. 75–176). Elsevier Ltd. https://doi.org/10.1016/j.pocean.2003.08.013

504 Lozier, M. S. (2012). Overturning in the North Atlantic. Ann. Rev. Mar. Sci. 4,
505   291–315. doi: 10.1146/annurev-marine-120710-100740

506 Lozier, M. S., Li, F., Bacon, S., Bahr, F., Bower, A. S., Cunningham, S. A., et al. (2019). A sea
507   change in our view of overturning in the subpolar North Atlantic, *Science*, 363, 516–521
508   http://science.sciencemag.org/

509 Marshall, J., & Schott, F. (1999). Open-ocean convection: Observations, theory, and models.
510   *Reviews of Geophysics*, *37*(1), 1–64. https://doi.org/10.1029/98RG02739

511 Pacini, A., Pickart, R. S., Bahr, F., Torres, D. J., Ramsey, A. L., Holte, J., et al. (2020). Mean
512   conditions and seasonality of the west Greenland boundary current system near cape
513   farewell. *Journal of Physical Oceanography*, *50*(10), 2849–2871.
514   https://doi.org/10.1175/JPO-D-20-0086.1

515 Palter, J. B., Lozier, M. S., & Lavender, K. L. (2008). How does Labrador sea water enter the
516   deep western boundary current? *Journal of Physical Oceanography*, 38(5), 968–983.
517   https://doi.org/10.1175/2007JPO3807.1

518 Pedlosky, J. (2003). Thermally Driven Circulations in Small Oceanic Basins. *Journal of Physical
519   Oceanography*, 33(11), 2333–2340. https://doi.org/10.1175/1520-
520   0485(2003)033<2333:TDCISO>2.0.CO;2

521 Pickart, R. S., & Spall, M. A. (2007). Impact of Labrador Sea convection on the North Atlantic
522   meridional overturning circulation. *Journal of Physical Oceanography*, *37*(9), 2207–2227.
523   https://doi.org/10.1175/JPO3178.1

524 Sayol, J. M., Dijkstra, H., & Katsman, C. (2019). Seasonal and regional variations of sinking in
525   the subpolar North Atlantic from a high-resolution ocean model. *Ocean Science*, *15*(4),
526   1033–1053. https://doi.org/10.5194/os-15-1033-2019

527 Send, U., & Marshall, J. (1995). Integral effects of deep convection. *Journal of Physical
528   Oceanography*, 25, 855–872

529 Spall, M. A. (2003). On the thermohaline circulation in at bottom marginal seas. In *Number 1
530   Journal of Marine Research* (Vol. 61)

531 Spall, M. A. (2004). Boundary Currents and Watermass Transformation in Marginal Seas.
532   *Journal of Physical Oceanography*, 34(5), 1197–1213. https://doi.org/10.1175/1520-
533   0485(2004)034<1197:BCAWTI>2.0.CO;2

534 Spall, M. A. (2008). Buoyancy-forced downwelling in boundary currents. *Journal of Physical
535   Oceanography*, *38*(12), 2704–2721. https://doi.org/10.1175/2008JPO3993.1

536 Spall, M. A. (2010). Dynamics of down welling in an eddy-resolving convective basin. *Journal
537   of Physical Oceanography*, *40*(10), 2341–2347. https://doi.org/10.1175/2010JPO4465.1

538 Spall, M. A., & Pickart, R. S. (2001). Where does dense water sink? a subpolar gyre example.
539   *Journal of Physical Oceanography*, *31*(3), 810–826. https://doi.org/10.1175/1520-
540   0485(2001)031<0810:WDDWSA>2.0.CO;2

541 Straneo, F. (2006). On the Connection between Dense Water Formation, Overturning, and
542   Poleward Heat Transport in a Convective Basin. *Journal of Physical Oceanography*, 36,
543   1822–1840. https://doi.org/10.1175/JPO2932.1

544 Suginohara, N. 1982: Coastal Upwelling: Onshore–Offshore Circulation, Equatorward Coastal
545   Jet and Poleward Undercurrent over a Continental Shelf-Slope. *Journal of Physical
546   Oceanography*, 12, 272-284

547 Szekely T., Gourrion J., Pouliquen S., Reverdin G. (2019). CORA, Coriolis Ocean Dataset for

548   Reanalysis. SEANOE. https://doi.org/10.17882/46219

549 Tagklis, F., Bracco, A., Ito, T., & Castelao, R. M. (2020). Submesoscale modulation of deep
550   water formation in the Labrador Sea. *Scientific Reports*, 10(1), 1–13.
551   https://doi.org/10.1038/s41598-020-74345-w

552 The NCEP/NCAR 40-Year Reanalysis Project: March, 1996 BAMS. National Centers for
553   Environmental Prediction/National Weather Service/NOAA/U.S. Department of Commerce.
554   1994, updated monthly. NCEP/NCAR Global Reanalysis Products, 1948-continuing.
555   Research Data Archive at NOAA/PSL: /data/gridded/data.ncep.reanalysis.html.

556 Våge, K., Pickart, R. S., Sarafanov, A., Knutsen, Ø., Mercier, H., Lherminier, P. et al. (2011).
557   The Irminger Gyre: Circulation, convection, and interannual variability. *Deep-Sea Research*
558   *Part I: Oceanographic Research Papers*, *58*(5), 590–614.
559   https://doi.org/10.1016/j.dsr.2011.03.001

560

561

562